



BNL-223508-2022-JAAM

# In Situ Studies of the Swelling by an Electrolyte in Electrochemical Doping of Ethylene Glycol-Substituted Polythiophene

L. Q. Flagg, R. Li

To be published in "ACS Applied Materials and Interfaces"

June 2022

Photon Sciences  
**Brookhaven National Laboratory**

**U.S. Department of Energy**  
USDOE Office of Science (SC), Basic Energy Sciences (BES) (SC-22)

Notice: This manuscript has been authored by employees of Brookhaven Science Associates, LLC under Contract No. DE-SC0012704 with the U.S. Department of Energy. The publisher by accepting the manuscript for publication acknowledges that the United States Government retains a non-exclusive, paid-up, irrevocable, world-wide license to publish or reproduce the published form of this manuscript, or allow others to do so, for United States Government purposes.

## **DISCLAIMER**

This report was prepared as an account of work sponsored by an agency of the United States Government. Neither the United States Government nor any agency thereof, nor any of their employees, nor any of their contractors, subcontractors, or their employees, makes any warranty, express or implied, or assumes any legal liability or responsibility for the accuracy, completeness, or any third party's use or the results of such use of any information, apparatus, product, or process disclosed, or represents that its use would not infringe privately owned rights. Reference herein to any specific commercial product, process, or service by trade name, trademark, manufacturer, or otherwise, does not necessarily constitute or imply its endorsement, recommendation, or favoring by the United States Government or any agency thereof or its contractors or subcontractors. The views and opinions of authors expressed herein do not necessarily state or reflect those of the United States Government or any agency thereof.

# In-situ studies of the swelling by electrolyte in the electrochemical doping of an ethylene glycol substituted polythiophene

*Lucas Q. Flagg,<sup>1</sup> Lauren E. Asselta,<sup>1</sup> Nicholas D'Antona,<sup>1</sup> Tommaso Nicolini,<sup>2</sup> Natalie Stingelin-Stutzmann,<sup>2,3</sup> Jonathan W. Onorato,<sup>4</sup> Christine K. Luscombe,<sup>5</sup> Ruipeng Li,<sup>6</sup> Lee J. Richter\*,<sup>1</sup>*

1 Materials Science and Engineering Division, National Institute of Standards and Technology,  
Gaithersburg, Md 20899, USA

2 Université de Bordeaux, CNRS Bordeaux INP/ENSCBP, Laboratoire de Chimie de Polymères  
Organiques UMR 5629, Allée Geoffroy Saint-Hilaire, 33615 Pessac Cedex, France

3 School of Materials Science & Engineering and School of Chemical & Biomolecular  
Engineering, Georgia Institute of Technology, 901 Atlantic Dr, Atlanta, GA, 30318, USA

4 Department of Materials Science and Engineering, University of Washington, Seattle,  
Washington 98195, USA

5 pi-Conjugated Polymer Unit, Okinawa Institute of Science and Technology Graduate University,  
1919-1 Tanacha, Onna-son, Kunigami-gun, Okinawa, 904-0495, Japan.

6 National Synchrotron Light Source II, Brookhaven National Laboratory, Upton, NY 11973, USA

## AUTHOR INFORMATION

### Corresponding Author

[\\*lee.richter@nist.gov](mailto:lee.richter@nist.gov)

**Keywords:** organic electrochemical transistors, organic electronics, organic semiconductors, organic mixed ionic electronic conductors, in situ diffraction, grazing incidence wide-angle scattering

### ABSTRACT

Organic mixed ionic electronic conductors (OMIECs) have the potential to enable diverse new technologies, ranging from biosensors to flexible energy storage devices and neuromorphic computing platforms. However, study of these materials in their operating state, which convolves both passive and potential driven solvent, cation, and anion ingress is extremely difficult, inhibiting rational materials design. In this report, we present a novel approach to the in-situ study of the electrochemical switching of a prototypical OMIEC, based on oligoethylene glycol (oEG) substitution of a semi-crystalline regioregular polythiophene via grazing-incidence X-ray scattering. By studying the crystal lattice both dry and in contact with electrolyte while maintaining potential control, we can directly observe the evolution of the crystalline domains and their relationship to film performance in an electrochemically gated transistor. Despite the oEG side chain enabling bulk electrolyte uptake, we find the crystalline regions are relatively hydrophobic, exhibiting little (less than one water per thiophene) swelling of the undoped polymer suggesting that the amorphous regions dominate the reported passive swelling behavior. With applied potential, we observe that the  $\pi$ - $\pi$  separation in the crystals contracts while the lamella spacing increases in a balanced fashion, resulting in negligible change in the crystal

volume. The potential induced changes in the crystal structure do not clearly correlate to electrical performance of the film as an organic electrochemical transistor, suggesting that the transistor performance is strongly influenced by the amorphous regions of the film.

## INTRODUCTION

Organic mixed ionic electronic conductors (OMIECs) have the potential to enable diverse new technologies,<sup>1-3</sup> ranging from biosensors<sup>4,5</sup> to flexible energy storage devices<sup>6,7</sup> and neuromorphic computing platforms.<sup>8,9</sup> As an electronic element, OMIECs enable organic electrochemical transistors (OECTs), where, unlike in the conventional field-gated thin-film-transistor (TFT), mobile carriers are induced in the bulk of the semiconductor and compensated by the ingress of electrolyte counter ions. The vast majority of OMIECs explored to date are based on polymers with semiconducting backbones where selectively engineered sidechains confer the desired functionality. The backbone structure is often that of an established organic semiconductor (OSC) such as regioregular polythiophene,<sup>10</sup> polydiketopyrrolopyrrole,<sup>11</sup> and polynaphthalene-diimide.<sup>12</sup> For the alkyl side chain versions of these polymers, the structure-function relationships are well understood in terms of a hierarchy of order. In general, interchain hopping is most facile and rapid charge transport is associated with minimal torsional disorder in the conjugated backbone,<sup>13</sup> that can be achieved by either synthesis (rigid motifs) or crystal packing.<sup>14</sup> For semicrystalline materials, intergrain transport is facilitated by amorphous cilia or tie-chains.<sup>15,16</sup> The two keys of local order and connectivity give rise to clear correlations between transport and both crystalline order and molecular mass.

In contrast to TFTs, where the capacitance of the gate dielectric and dielectric breakdown typically limit carrier densities to  $\approx 10^{19}$  cm<sup>-3</sup>, OECTs can often achieve carrier densities approaching 10<sup>21</sup> cm<sup>-3</sup>.<sup>2</sup> Therefore, their behavior is often correlated to that of chemically doped films, that have been studied extensively, particularly in the context of thermoelectrics.<sup>17</sup> One of the most extensively studied OSCs, both field-gated (TFT) and doped, is regioregular poly-3-hexylthiophene (P3HT). When operated as a TFT, P3HT devices typically exhibit a mobility,  $\mu$ ,

of ( $10^{-3}$  to  $10^{-2}$ )  $\text{cm}^2/(\text{V s})$ . It is notable that, when highly doped, P3HT exhibits a mobility  $> 10^{-1}$   $\text{cm}^2/(\text{V s})$ .<sup>18</sup> This increase in mobility with doping has been attributed to trap filling in variable range hoping transport<sup>18</sup> or a structural transition in the crystalline domains, driven by counter-ion insertion.<sup>19</sup> Similar high mobilities (relative to TFT controls) are reported for OECTs.

The operational state of an OECT differs from a dry TFT due to direct contact with an electrolyte, which enables solvent (swelling),<sup>20</sup> anion,<sup>21</sup> and cation<sup>22</sup> ingress. These species can stress/modify the structure in both the crystalline and amorphous regions of the film. A number of recent reports highlight the importance of both passive and active (bias driven) swelling on both the device performance and cycling stability.<sup>23,24,25</sup> Most of these studies have been limited to probing the bulk film swelling via quartz-crystal microbalance (QCM) due to the difficulty of interrogation of the crystal lattice in contact with electrolyte. Many OECT studies show the effect of ex-situ doping via grazing-incidence wide-angle X-ray scattering (GIWAXS) but dry OMIECs do not always map well to the real operating conditions.<sup>26</sup> This discrepancy has two origins. First, the lack of electrolyte obscures the real operational state. Second, there are time dependent relaxation effects after the bias is removed and films are removed from solution, especially for n-type materials, but also relevant for p-type materials. Thus, it is *critical* to rational materials design, that in-situ/in-operando techniques be developed to characterize OMIECs in contact with electrolyte and with active potential application.<sup>27</sup>

In-situ X-ray scattering of electrified interfaces, under potential control and in contact with electrolyte has an extensive history for hard X-ray scattering of inorganic interfaces.<sup>28</sup> Typical designs are of a plunger<sup>29</sup> or inflatable window design.<sup>30-32</sup> The key trade-off in the design of in-situ X-ray scattering cells involves having adequate solution access to the interface of interest to enable electrochemical switching (by minimizing series resistance), while reducing the

electrolyte path length to minimize the interference from the amorphous halo of the (typically aqueous) electrolyte. To effectively study doping in semicrystalline polymer materials, it is critical to be able to access the  $\pi$ - $\pi$  stacking feature, typically at  $\approx 1.7 \text{ \AA}^{-1}$ , and the lamella scattering feature, typically  $\approx 0.3 \text{ \AA}^{-1}$ , at device relevant thicknesses ( $\approx 100 \text{ nm}$ ) while in contact with electrolyte. Unfortunately, the  $\pi$ - $\pi$  feature often lies directly in the region of water scattering. Here we highlight recent designs for *in situ* X-ray studies of OMIECs. All designs are based on grazing-incidence configurations, due to the weak scattering by the thin polymer films. Bischak, et al. designed an inverted geometry where the X-ray probes through a thin gold substrate in contact with electrolyte on the far side. This provides potential control and electrolyte contact but the unwanted scattering/absorption of the Kapton/gold obscured access to the  $\pi$ - $\pi$  feature.<sup>33</sup> Paulsen et al. presented a “cone cell” that radially limits the extent of electrolyte (and thus path length); however, clear observation of the film  $\pi$ - $\pi$  stacking requires film thickness similar to the x-ray beam height ( $\mu\text{m}$ ) for clear contrast. Recently, a cell based on a porous (frit) substrate has been presented that allows free X-ray access to all peaks of interest by allowing direct contact to the electrolyte only from the bottom of the film.<sup>34</sup> The frit design is conceptually simple, but requires humidity control on the non-electrolyte film face, transfer of the films from non-porous substrates, and exhibits electrochemical nonidealities from the stainless steel frit. Similar to the frit design, studies have been performed with films on top of polymeric electrolytes<sup>19</sup> in a reflection configuration, eliminating electrolyte swelling, but allowing potential controlled doping. Each of these represents a valuable contribution to the field but suffers certain limitations including lack of access to the  $\pi$ - $\pi$  scattering feature, requirement of unusually thick films ( $\approx \mu\text{m}$ ), difficult/abnormal film preparation, or ill-defined potential.

In this report, we present an approach to in-situ studies of OMIEC films, based on a simple modification of a low-angle blade coater, commonly used for real-time studies of film formation from solution.<sup>35</sup> We apply it to the study of the electrochemical doping of poly(3-[2-(2-methoxyethoxy)ethoxy]methyl}thiophene-2,5-diyl) (P3MEEMT, see Figure 1 A), a recently introduced semicrystalline polymeric OMIEC, based on the regioregular polythiophene backbone of P3HT, distinguished by the presence of hydrophilic, oligoethylene oxide (oEG) side chains. In earlier studies,<sup>10</sup> P3MEEMT exhibits a material figure<sup>36</sup> of merit,  $\mu C^*$  where  $C^*$  is the volumetric capacitance, of 49 F/(cm V s) in KCl, on par with ethylene glycol treated poly(3,4-ethylenedioxythiophene):poly(styrenesulfonate), PEDOT:PSS.<sup>36</sup> To achieve high doping levels, we focus on hexafluorophosphate ( $PF_6^-$ ) as the counter ion,<sup>10,21,37</sup> but complement the study with the more biologically relevant  $Cl^-$ .

## RESULTS AND DISCUSSION

Shown in Figure 1 is a schematic of our system. Conceptually, it is similar to a scanning electrochemical cell<sup>38</sup> and we refer to it here as a ‘rolling drop’ electrode. The electrolyte of interest is trapped between the film (cast on a p++ silicon substrate that acts as the working electrode) and the blade of a low-angle blade coater.<sup>39</sup> The underside of the glass blade is silver coated and converted to Ag/AgCl by exposure to bleach to serve as both the counter and quasi reference in a 2 electrode configuration. Thus, application of the desired potential across the film is nominally identical to the conditions of OECT device testing with standard Ag/AgCl pellet gate electrodes. A typical measurement cycle consists of placing the drop covered sample at the position of the incident beam for a grazing-incidence wide (or small)-angle scattering measurement. Potential is applied and the system is allowed to achieve steady state (typically 60 s to 120 s). While the blade is directly over the X-ray spot, the shadow of the blade on the

detector prevents out-of-plane X-ray measurements (Figure 1A). This is addressed by translating the blade laterally away from the measurement spot (Figure 1B) while continuously collecting scattering patterns (at 0.1 Hz in this study), allowing access to a full  $\pi/2$  scattering angle. As the blade translates, the meniscus of the electrolyte passes over the measurement spot, effectively tuning the electrolyte thickness in time. In practice, this is done as a kinetic sweep: the drop is translated completely off the X-ray measurement spot, going from fully hydrated (in contact with bulk electrolyte) to nominally dry (in contact with room relative humidity) (Figure 1C). To date, all materials studied with this method (over 10 different modified organic semiconductors) are sufficiently hydrophobic that the drop stays attached to the receding blade and a wetted film is not created. However, it does require that the film be stable to the transit of the air-electrolyte interface. We have found that, in general, polar side chain polymer films are prone to delamination from the substrate, but a moderate (75 °C for 20 min) anneal creates adequate adhesion to perform the rolling drop measurement. Simultaneously, we collect normal-incidence visible reflectance data as a direct measurement of both doping state and swelling.

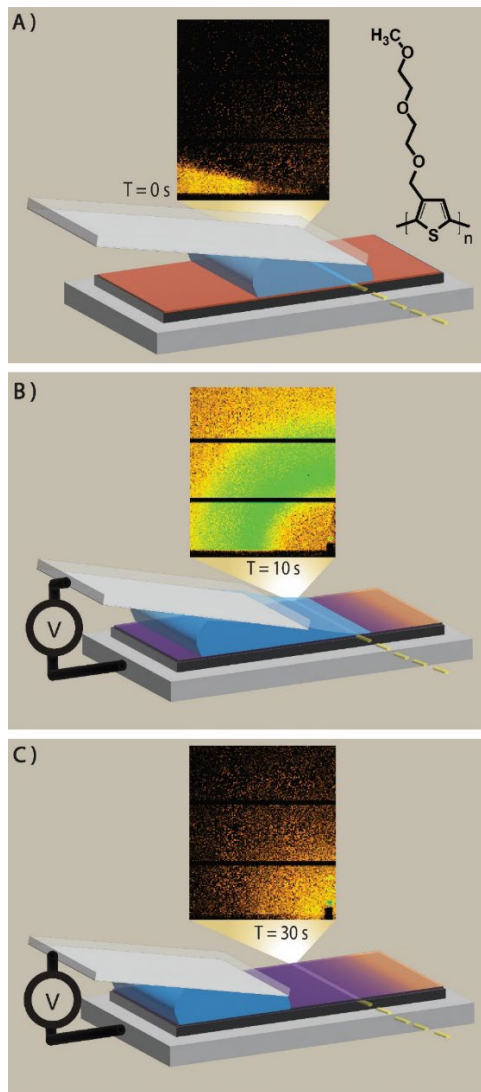


**Figure 1.** A through C: schematic of the operation of the “rolling drop” electrode, following the dynamic reduction of the electrolyte layer thickness after establishing steady state. 2D images are typical wide-angle X-Ray scattering patterns. The blade angle ( $\approx 5^\circ$ ) has been exaggerated in the schematic. A) Initial condition, blade shadows the out-of-plane scattering. Inset: structure of P3MEEMT. B) Early times, blade no longer shadows out-of-plane scattering, but significant electrolyte thickness contributes an amorphous halo to the scattering. C) Late times, meniscus has completely passed the measurement area and the sample is dry (in contact with room relative humidity).

Using this rolling drop configuration, we comprehensively examine the swelling of the lattice of P3MEEMT. Shown in Figure 2A is the 2D GIWAXS pattern for a high number-average molar mass ( $M_n$ ) 78 kg/mol P3MEEMT (dispersity,  $M_w/M_n$ , 1.47), annealed at 115 °C. These conditions result in textured films with a bimodal distribution of predominantly face-on lamellar crystals with highly ordered (relatively sharp) diffraction features. While the crystal structure of P3MEEMT is not known, we will adopt a notation consistent with the reported  $P2_1/c$  unit cell for P3HT.<sup>40</sup> Due to the two chains in the unit cell, the first non-zero  $\pi$ - $\pi$  diffraction feature is the (020). We note in passing that for films with the c-axis in-plane (as are formed here, confirmed by ellipsometry Figure S1), the out-of-plane (020) has no interference from a possible (001), unlike the commonly observed in-plane feature for edge-on P3HT.<sup>41</sup> We will adopt the notation of  $q_{hkl}$ , where h, k and l, are Miller planes indices, when referring to the q-space position of diffraction features.

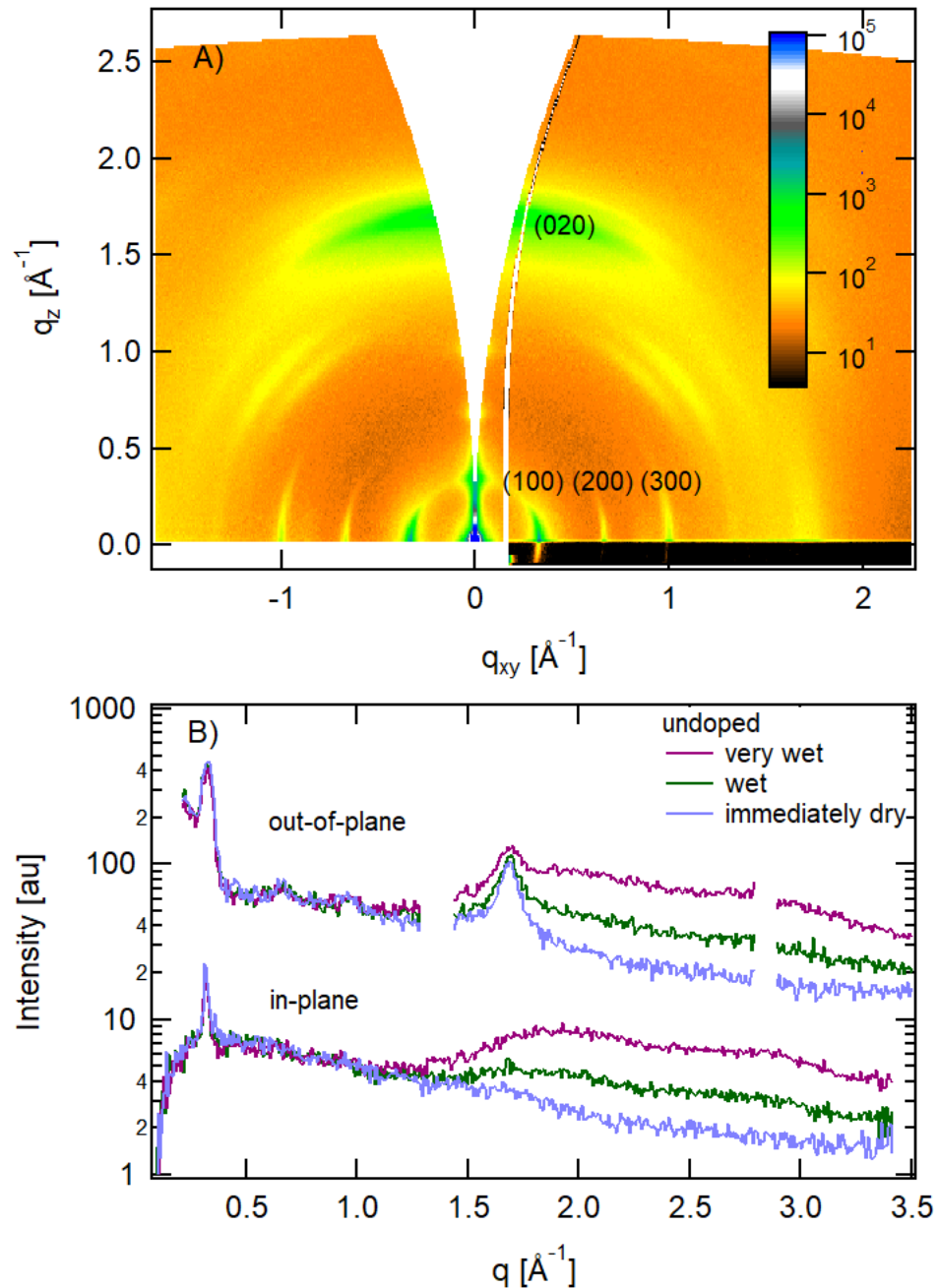


**Figure 2.** A) Ex-situ GIWAXS pattern from P3MEEMT. in-plane (h00) series and out-of-plane (020) of the face-on material are labeled. B) in-plane and out-of-plane sector cuts from select stages of the drop transit through the X-ray beam. Broad scattering at ( $\approx 1.8$  and  $\approx 2.8$ )  $\text{\AA}^{-1}$  is due to water.

We first focus on the changes in the polymer upon exposure to electrolyte (passive swelling) in the neutral state. We have performed complementary studies of the bulk volumetric swelling via spectroscopic ellipsometry in contact with controlled relative humidity (RH, Figures S2-S3) and liquid water (Figure S4). Nominally 100 % RH results in  $\approx$ 10% thickness swelling, while contact with liquid results in  $\approx$  18% swelling; an example of Schroeder's paradox.<sup>42,43</sup> The liquid swelling is consistent with values previously reported.<sup>10</sup> Figure 2B shows select diffraction sector cuts from the time domain evolution of an undoped film during one kinetic blade passage highlighting 3 peaks of interest: the in-plane lamella (100), the out-of-plane  $\pi$  (020) and the broad water scattering feature. Full kinetic results are shown in Figure S5. At early time (Figure 1A) the blade obscures the out-of-plane scattering pattern. As the blade shadow withdraws but the film is still in direct electrolyte contact (Figure 1B, red trace in Figure 2B), the in-plane lamellae are easily visible because they do not overlap with the amorphous halo of water scattering. However, the broad water scattering feature obscures the (020) peak. By choosing a time when the electrolyte is still present but thin (green trace in Figure 2B), we can analyze the peak position while the film is in contact with electrolyte, but the peak is strong enough above the background to reliably analyze its position. Finally, as the blade withdraws to its furthest extent (mm beyond the X-ray measurements spot), we see a “dry” spectrum (Figure 1C, blue in Figure 2B). Here the film is in equilibrium with room humidity, which gives the strongest GIWAXS peaks but loses the electrolyte effect as seen by the slight contraction in the (100) direction (see Figure 3B). By careful choice of the time window averaged, we can extract the swollen lattice parameters with high fidelity as well as contrast it with the dry state of the film. We note that, while the rolling drop is removed from the measurement region in the retracted position, lateral conductivity in the film appears sufficient to maintain the nominally dry, doped

state. This is confirmed by studies with 0.1 mol/L KCl as the electrolyte. We found that Cl<sup>-</sup> doped films were unstable, spontaneously dedoping in about 5 min, as observed by visible color change and by both ex-situ ellipsometry and ex-situ GIWAXS (Figure S6). However, clear evidence of the doped state is observed in both white-light interferometry (Figure S17) and GIWAXS (Figure S15 and S16) in the rolling drop experiment, with the drop a few mm from the measurement region.

Unlike the volumetric swelling, there was no significant difference in  $q_{100}$  swelling in  $\approx 100\%$  RH (Figure S7, Table S1), or liquid water (Figure 2). In both cases, only a (3 to 4) % expansion of the lattice is observed. Notably for P3MEEMT, under all conditions (RH, liquid, and doping level, see below) there is no distinguishable change in the  $q_{020}$  associated with the presence of electrolyte, i.e. there is no detectable *electrolyte* swelling of the  $\pi$ - $\pi$  stacking. Additionally, there is no significant change in crystalline order, as reflected in either the diffraction widths or amplitudes, indicating the electrolyte does not disrupt or enhance the existing crystal structure. The change in the  $q_{100}$  of (3 to 4) % is significantly smaller than the film volumetric swelling (10 to 18) %, clearly establishing that the majority of the volumetric expansion occurs in the amorphous regions of the film. Assuming the P2<sub>1</sub>/c structure with two chains per unit cell (four thiophenes) proposed for P3HT,<sup>40</sup> and no changes in the crystal angles upon swelling, the undoped unit cell volume increases by  $\approx 40\text{ \AA}^3$  in contact with electrolyte. This corresponds to  $\approx 1/3$  of a water molecule ( $30\text{ \AA}^3$ ) per monomer. Thus, despite the polarity of the side chains, the crystalline regions are relatively hydrophobic in the neutral state. We note that the incompressibility assumption may underestimate the amount of water in the side chains, due to the conformation flexibility of the side chains.

Next, we present the effect of potential on the lattice, as shown in Figure 3. This is done as subsequent blade passages with a different potential for each blade passage. We first focus on the behavior of the  $q_{020}$ . As is often observed for doped P3HT<sup>19,44,45</sup> the  $q_{020}$  is observed to increase, indicating a contraction of the  $\pi$ - $\pi$  separation above a critical potential/induced charge density. As there is no evidence for changes in the (020) due to electrolyte swelling, here we analyze films with minimal electrolyte interference for high quality, as shown in Figure 3. There is no clear isosbestic point in the data, implying that at intermediate potentials (-0.30 V vs. Ag/AgCl) the system evolves as a continuous alloy, not as distinct undoped and doped phases.<sup>33</sup> We note that, in order to maintain a consistent sign convention between the in-situ studies and OECT device studies (see below), we report all potentials relative to a Ag/AgCl quasi-reference with the film grounded. From Figure 3A, it is apparent that there are no significant changes in either relative (020) crystallinity, nor crystal size (coherence length), with doping. Diffraction feature widths from line fits are presented in table S2. This is in contrast to reports of enhanced ordering upon doping of regiorandom P3HT.<sup>41</sup> The face-on crystals in these films (annealed at 115 °C) exhibit high levels of order as prepared: the (100) coherence length,  $l_c=2\pi/\text{FWHM}$  (FWHM=fullwidth at half maximum), can exceed 30 nm while the (020)  $l_c$  can exceed 8 nm; therefore, additional ordering may not be detectable. Unfortunately, studies of unannealed films, with lower initial order, were confounded by delamination.

Shown in Figure 3B is the evolution of the (100). In contrast to the  $q_{020}$  contraction, a small  $\approx 3\%$  expansion of the lamella is observed, again at  $\approx -0.3$  V. This is in addition to the  $\approx 3\%$  expansion due to the electrolyte, such that the doped, swollen film expands a total of  $\approx 5\%$ .

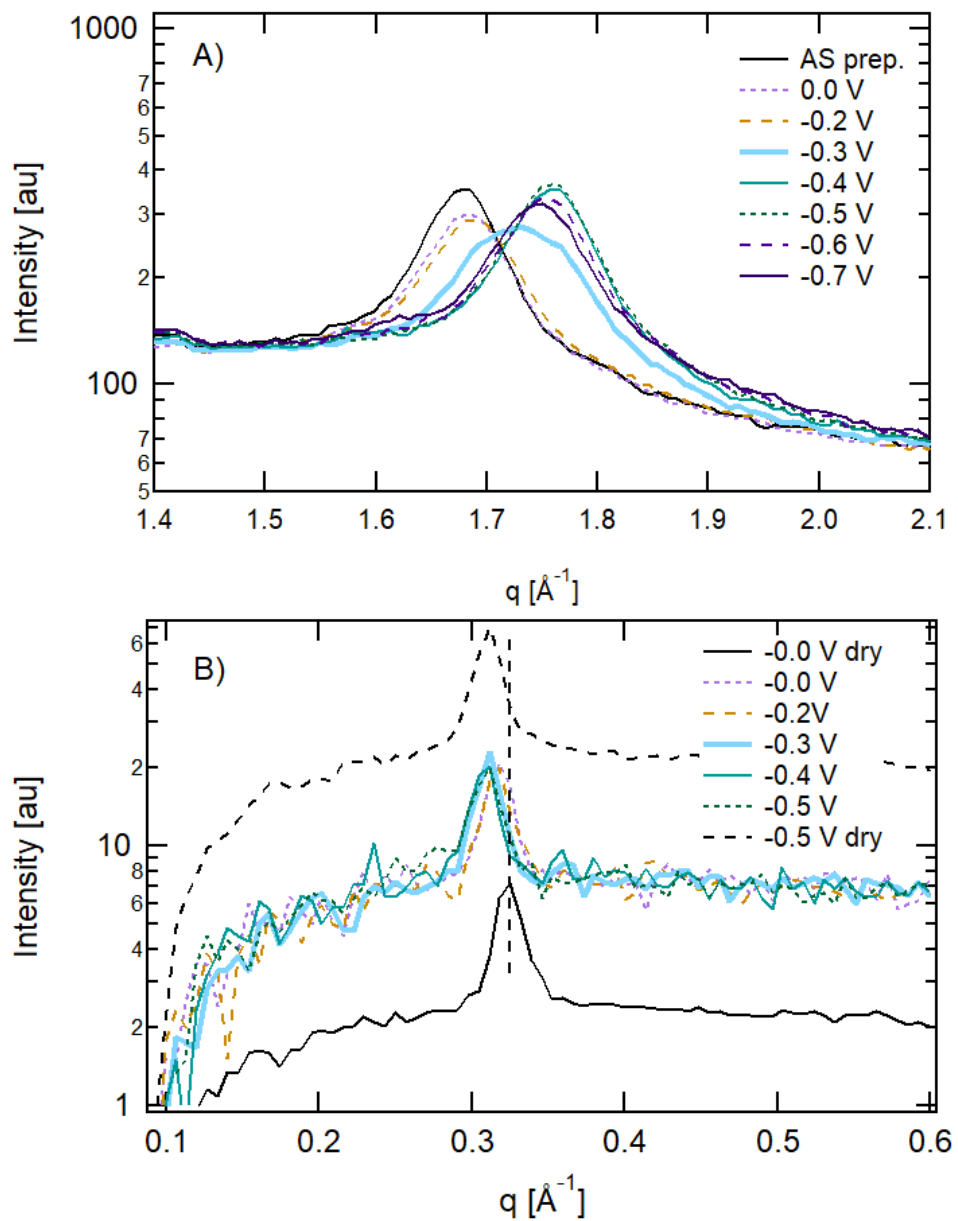


Figure 3 A) Detail of the out-of-plane (020) feature vs applied potential (vs Ag/AgCl, uncorrected) in 0.1 mol/L KPF<sub>6</sub>. Note the absence of an isosbestic point. B) Detail of the in-plane (100) feature

vs applied potential. Color are films in contact with electrolyte (wet); black are films with electrolyte removed (room RH). Note both the subtle swelling by hydration, and by doping.

Using the rolling drop electrode, we are able to, at the same exact location of a single film, characterize four distinct conditions: undoped vs doped, dry (room relative humidity  $\approx 35\%$ ) vs in contact with liquid (wet). In table 1 we summarize the behavior of the face on crystals (in-plane lamella (100) and out-of-plane  $\pi$ - $\pi$  (020)) for these four states, and the relative changes upon doping and swelling. The prominent observation in lattice spacing is a sharp contraction of the  $\pi$ - $\pi$  spacing of 3 % at -0.2 V, accompanied by a (2 to 3) % expansion of the lamella separation,  $d_{100}=2\pi/q_{100}$ . The very small doping induced change in the  $q_{100}$  implies that, contrary to the  $\approx 3\%$  change in the undoped unit cell volume upon hydration, the volume of the unit cell does not change significantly upon doping; the small additional (100) expansion is compensated by the (020) contraction. The dry film expands immeasurably, while the wet film *contracts* by  $25\text{ \AA}^3$ , to be compared with a  $\text{PF}_6^-$  ionic volume of  $65\text{ \AA}^3$ .

**Table 1.** Comparison of characteristic diffraction features upon hydration and doping with 0.1 mol/L  $\text{KPF}_6$  at -0.5 V relative to  $\text{Ag}/\text{AgCl}$ .

(100)	dry $q/\text{\AA}^{-1}$	Change %	Wet $q/\text{\AA}^{-1}$	dry $\text{FWHM}/\text{\AA}^{-1}$	Change %	Wet $\text{FWHM}/\text{\AA}^{-1}$
Undoped	.331 $\pm$ .001	-3 $\pm$ 1	.322 $\pm$ .004	.018	0	.018
% change	-3 $\pm$ 1		-2 $\pm$ 1	0		0
Doped	.322 $\pm$ .001	-2. $\pm$ 1.	.314 $\pm$ .001	.018	0	.018
<hr/>						
<b>(020)</b>						
Undoped	1.683 $\pm$ .002	0 $\pm$ 1	1.684 $\pm$ .002	.097	1 $\pm$ 4	.098
% change	3 $\pm$ 1		3 $\pm$ 1	2 $\pm$ 4		1 $\pm$ 4
Doped	1.758 $\pm$ .002	0 $\pm$ 1	1.757 $\pm$ .002	.095	2 $\pm$ 4	.097

Uncertainties are 1 standard deviation based on the covariance matrix of the peak fits.

In Figure 4, we compare the structural metrics ( $q_{100}$  and  $q_{020}$ ) as a function of applied potential with device data from independently characterized OECTs (see Figure S8 through S11). We use the normal-incidence white-light-interferometry recorded simultaneously with the in-situ GIWAXS and spectroscopic ellipsometry recorded contemporaneously with the device measurements to assure comparison at the same doping level (Figure S12 & S13). We find a nominal 0.1 V offset must be applied to the in-situ GIWAXS potential to agree with the device data. This shift has been applied to the diffraction data in Figure 4. We attribute this to trace oxidation of the polymer dependent on casting solution age and not to differences in the Ag/AgCl reference (pellet vs thin film). While the  $\pi$ - $\pi$  spacing is invariant with increased doping above a threshold, the  $d_{100}$  appears to relax (deswell) at higher injected charge density. This deswelling is also observed for the out-of-plane (100) (see Figure S14), but it is not observed in KCl (see Figure S15). However, one cannot achieve as high of injected charge density in KCl. Similar deswelling at high charging has been reported for PEDOT:PSS<sup>26</sup> and might be reflective of bipolaron formation, although beam damage of the highly doped film cannot be excluded.

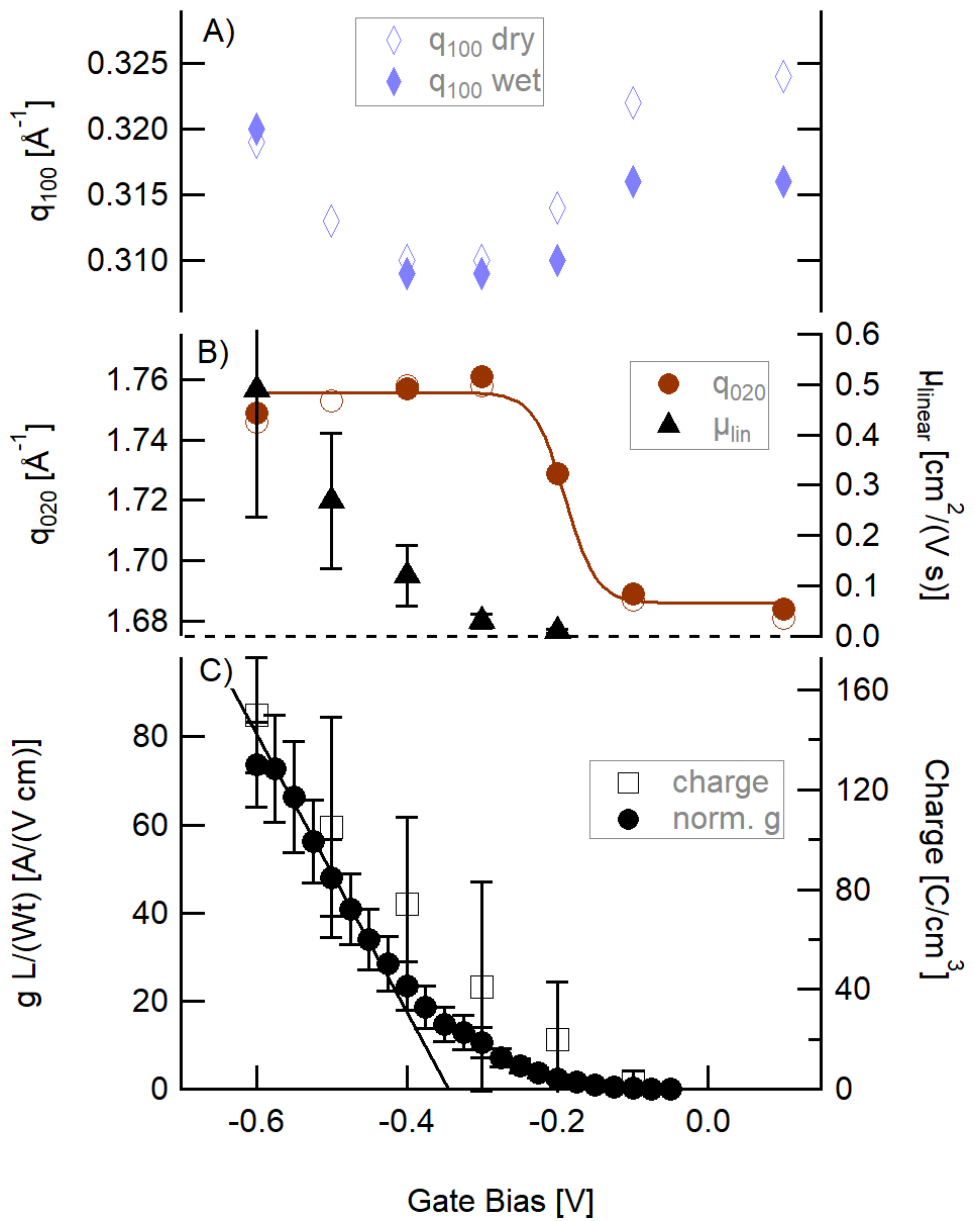


Figure 4 A) Hydrated/wet (closed) and dry (open) scattering magnitude for the  $q_{100}$  (blue) and B)  $q_{020}$  (red) features as a function of gate bias showing the lamellar expansion (decrease in  $q_{100}$ ) and pi contraction (increase in  $q_{020}$ ) as the film is oxidized. Line is a sigmoid-fit guide-to-the-eye. C) Also shown are the linear mobility, the normalized transconductance [ $g \text{ L}/(\text{Wt}) \text{ Å}/\text{cm}$ ] averaged over 8 devices from OECTs with thickness ranging from (74 to 114) nm and channel length ranging from

(82 to 397)  $\mu\text{m}$ , and the charge-per-unit volume from chronocoulometry. GIWAXS potential has been corrected as described in the text.

There have been extensive studies, both ex-situ and in-situ, of P3HT doped with either bis(trifluoromethane)sulfonimide, TFSI, or 2,3,5,6-Tetrafluoro-7,7,8,8-tetracyanoquinodimethane, F4TCNQ, either by vapor, solvent exchange, or with polymer electrolytes, so effectively ‘dry’. Common to all studies is a contraction of the  $\pi$ - $\pi$  and expansion of the lamella above some critical doping/charging level. The work most directly comparable to the present study is that of Thomas et al.,<sup>19</sup> who used a polymer electrolyte (thus prohibiting electrolyte swelling) to enable TFSI doping of P3HT. They report a sharp, 4% contraction of the (020) at a charge density of  $\approx 5 \cdot 10^{20} \text{ h/cm}^3$  (h=hole), or  $95 \text{ C/cm}^3$ , similar to the  $\approx 40 \text{ C/cm}^3$  accumulated charge at -0.2 V (corrected) in Figure 4. However, unlike the negligible volumetric swelling observed with  $\text{PF}_6^-$  in P3MEEMT in the presence of electrolyte, TFSI doping results in a 12 % expansion of the (100) in P3HT and a  $\approx 80 \text{ \AA}^3$  increase in the unit cell volume. In the work of Thomas et al., the crystal changes ( $\pi$ - $\pi$  contraction and (100) expansion) were attributed to a phase change due to the ingress of dopant ions above a critical charging density. Importantly, the crystal structure change directly correlated with a step-like increase in the film mobility. As discussed in the introduction, the mobility of polythiophenes generally increases exponentially with increasing doping level, and plateaus at charge levels  $\approx 5 \cdot 10^{20} \text{ h/cm}^3$ .<sup>46</sup> In Figure 4, it is clear that, while the crystal morphology changes at a potential similar to the transistor threshold, the device mobility is still increasing significantly beyond the saturation of changes in the crystal structure. This suggests that transport in the P3MEEMT devices is more influenced by the amorphous domains, relative to previous studies of P3HT. We note that, while P3MEEMT films clearly contain highly oriented material, the GIWAXS does not provide

absolute crystallinity. Thus, the crystal fraction in P3MEEMT may be less than the typical 50 % found in P3HT.<sup>47</sup> The evolution of the total film charge, monotonically increasing throughout the studied potential range, and the in-situ GIWAXS, saturating at moderate potential, is consistent with the observation of Thomas et al.<sup>19</sup> that doping initially modifies the crystals (polarons are more stable in the highly ordered material) and subsequently dopes the amorphous material. Unlike P3HT, this cannot be confirmed by spectroelectrochemistry, as there are no distinct features (vibronic progression) attributable to the crystalline P3MEEMT.<sup>10</sup>

Shown in Figure S15 and S16 are comparable data for doping in 0.1 mol/L KCl. Consistent with earlier reports of device threshold shifts,<sup>10</sup> the KCl doped crystals change at nominally 200 mV deeper potentials. Except for the potential shift, there are no significant differences in either the hydration or doping induced structural changes between KPF<sub>6</sub> and KCl electrolytes. It is notable that there is no significant difference in the crystal volumetric swelling between PF<sub>6</sub><sup>-</sup> (Figure 3 and S14) and Cl<sup>-</sup>. In studies of total mass uptake by QCM,<sup>10</sup> it was noted that films took up nominally 7 waters for each Cl<sup>-</sup>, or an ‘active swelling’ of  $\approx$ 10 % by mass in addition to the passive swelling of  $\approx$ 20 %. There is no evidence for increased electrolyte uptake for the Cl<sup>-</sup> doped crystalline material, emphasizing the relatively hydrophobic nature of the crystals. Similarly, based on QCM,<sup>10</sup> PF<sub>6</sub><sup>-</sup> is a dehydrating (hydrophobic) ion, leading to mass *loss* upon doping due to water ejection from the passively swollen film.<sup>10</sup> It is unambiguous that the *crystalline* material, whether doped with Cl<sup>-</sup> or PF<sub>6</sub><sup>-</sup>, does not exhibit significant ‘active’ or additional, bias driven swelling. This is in dramatic contrast to the bulk of many OMIEC films that are known to swell up to 100 % in response to doping,<sup>23</sup> and frames swelling of OECTs as a complicated effect that varies widely between the amorphous and crystalline fractions of films. It is also notable that, unlike the case of TSFI in P3HT (12 % expansion of lamella)<sup>19</sup> or F4TCNQ in P3HT (11 % expansion of the

lamella)<sup>48</sup> there is little ( $\approx 3\%$  expansion) change in the lamella upon incorporation of  $\text{PF}_6^-$ , in spite of similar ion volumes and doping levels. This suggests that the (presumed mostly amorphous) oEG side chains of P3MEEMT may be more conformationally forgiving and are capable of accommodating the strain from both the ion volume and the 3 % compression in the  $\pi$ - $\pi$  direction more readily than the shorter alkyl of P3HT. It is interesting to note that for the in-plane  $q_{100}$ , the swelling of the  $\text{PF}_6^-$  doped film by electrolyte is undetectable; however, this trend is not reflected in the out-of-plane  $q_{100}$  (See Figure S14). Whether this is reflective of confinement in the face-on crystals, or spurious correlation in the subtle data cannot be determined.

## CONCLUSION

In this manuscript we introduce a novel method for observing the crystal lattice of OMIECs in direct contact with electrolyte and potential by modifying a commonly used blade-coater. With each blade passage we interrogate the electrolyte swollen crystal lattice and the dry lattice at a given potential. Using this method, we can extract both the hydrated and dry lattice parameters, both in- and out-of-plane. By performing kinetic traces at multiple potentials, we can separate the effect of electrolyte swelling from that of the bias driven swelling. For P3MEEMT, we observe minimal ( $< 5\%$ ) crystal swelling compared to the bulk ( $\approx 20\%$ ) swelling of the film, implying that the electrolyte predominantly resides in the amorphous content of the film. The doping induced changes in crystal structure: contraction in the  $\pi$ - $\pi$  direction and expansion of the lamella separation with negligible change in crystal volume, saturates well before either the total film charge or device mobility. Overall, this technique provides unique insight into the swollen structure of OMIECs and has a valuable role in the suit of characterization techniques that have been developed.

## EXPERIMENTAL SECTION

### Materials and film Deposition

poly(3-{[2-(2-methoxyethoxy)ethoxy]methyl}thiophene-2,5-diyl), P3MEEMT, was synthesized as described previously.<sup>10</sup> Based on high performance liquid chromatography in tetrahydrofuran, the number average molar mass (Mn) was 78 kg/mol and the mass average molar mass (Mw) 115 kg/mol, with dispersity, Mw/Mn, of 1.47. All electrolyte solutions were prepared with 18 MΩ, millipure water. KCl from Sigma and KPF<sub>6</sub>, provided by Dr. Thomas Moffat, were used as received.

All substrates (p++ doped Silicon for X-ray diffraction or ellipsometry, glass for devices) were cleaned by 10 min ultrasonic agitation in each of chloroform and isopropyl alcohol, followed by ultraviolet-ozone treatment for 10 min. P3MEEMT was deposited by blade coating with a custom, low angle coater described in Ref. 39. The blade height was 200 μm and the blade speed nominally 40 mm/s. Substrate temperature was 30 °C. Blade speed was varied to produce variable film thickness. The solution was 20 mg/mL in chlorobenzene. Solution was dissolved at 50 °C with stirring and allowed to cool to room temperature. Typical film thickness was 75 nm.

### Organic Electrochemical Devices

OEET devices were prepared on Au bottom contact devices with nominal channel lengths of (100, 200, 300, or 400) μm and channel widths of 1 mm, created by vapor deposition through a shadow-mask on a glass substrate. Nominally 50 nm of Au was deposited on a 10 nm Cr adhesion layer. After deposition of the polymer film, excess material was removed by manual scrubbing to limit the material to the nominal channel region. A polydimethylsiloxane well was adhered to the chip and filled with ≈ 350 μL of electrolyte. A Ag/AgCl pellet electrode was used as the gate. A Keithley 2632 dual channel source meter was used to record the gate and drain currents as a function of gate and source potential. μ C\* and V<sub>th</sub> were obtained from the saturation characteristics of the numerically computed transconductance:

$$g = \frac{d I_D}{d V_{GS}} = \mu C^* \frac{W t}{L} (V_{th} - V_{GS})$$

where  $I_D$  is the drain current,  $V_{GS}$  the gate potential,  $V_{th}$  the threshold voltage,  $C^*$  the volumetric capacitance,  $\mu$  the mobility,  $W$  is the channel width,  $t$  film thickness,  $L$  channel length. The film thickness was determined by spectroscopic ellipsometry (in the dry state) and the channel dimensions determined by optical microscopy, for each device.

In the linear regime, the channel current is given by

$$I_D = \rho \mu \frac{W t}{L} V_{DS}$$

where  $\rho$  is the charge in the channel and  $V_{DS}$  the applied voltage. Linear mobilities were extracted from the gate-current-corrected, low  $V_{DS}$  region of output-curves, at  $V_{GS} \geq 0.2$  V.

### Chronocoulometry

The charge density in the film was determined by integrated chronocoulometry, based on measured film area, following the procedures of Ref. 37.

### Grazing Incidence Wide Angle X-Ray scattering (GIWAXS)

GIWAXS was performed at the 11-BM CMS beamline at NSLS-II. A beam energy of 13.5 keV was used for all measurements. Sample-to-detector distance and beam center were determined from a silver behenate standard. The vertical center was shifted to produce out-of-plane (h00) series with no extrapolated offset. This empirically corrects for both the shift in the incident Poynting vector due to the standing wave at grazing incidence, and for the refractive index correction upon exit. Ex-situ data was taken with a Pilatus 800K detector, with the sample in vacuum. In-situ data (both rolling drop and solvent vapor annealing) was taken in air, with a Pilatus 300K detector. Solvent vapor annealing was done in a custom cell, sealed with Kapton windows, kindly provided by Dr. Ben Ocko. The cell allowed up to 9 samples to be measured in parallel. Water vapor was controlled by a mixed stream of pure nitrogen and nitrogen saturated with water vapor via a bubbler. A very large volume bubbler was used to limit the evaporative cooling of the liquid water. Relative humidity was recorded by a sensor in the cell, and consistent with vapor flow mixing rates and 100 % saturation.

Rolling Drop GIWAXS was performed as described in the main text. Typically, 300 nm of Ag was deposited on a glass slide (blade) with a 10 nm Cr adhesion layer, and converted to Ag/AgCl by exposure to 4 % bleach for 2 min. The blade-sample gap was typically 300  $\mu$ m and nominally 500  $\mu$ L of electrolyte was dispensed between the blade and substrate to form the drop. The blade-sample potential was controlled by an EG&G PAR 363 potentiostat, under analog control by custom software developed by NSLS-II.

### Spectroscopic Ellipsometry (SE)

SE was performed with a JA Woollam CO M2000-D spectroscopic instrument, nominally spanning (200 to 1700) nm. A custom cell was used for both vapor exposure and liquid exposure. The long liquid path length limited the wavelength range to nominally (300 to 1000) nm. Water vapor was controlled by a mixed stream of pure nitrogen and nitrogen saturated with water vapor via a bubbler. Relative humidity was recorded by a sensor in the cell, and consistent with vapor flow mixing rates and an RH of (98 to 99) % at saturation. CompleteEase software was used to correct for any birefringence of the cell windows and for analysis. For SVA, a uniaxial model was fit to the initial, dry film, and then all subsequent data was fit to an EMA mixture of the dry dielectric function and water, allowing volume fraction and thickness to independently vary.

### White-Light Interferometry (WLI)

Concurrent with the rolling-drop GIWAXS measurements, WLI was performed at normal incidence on the same location on the sample as the diffraction measurements, when the drop had cleared and there was no obstruction. This provides immediate feedback on the doping of the film. The custom system is based on a 6 around 1 fiber for illumination/collection, a deuterium/quartz-tungsten halogen broad-band source, and a Si diode-array detector. The reflectance spectra, corrected by reference to the reflection from a native oxide covered Si chip, was analyzed in the CompleteEase software.

## ASSOCIATED CONTENT

### Supporting Information.

The Supporting Information is available free of charge at #####.

Figures S1 through S17, Table S1 and S2. Example time-dependent GIWAXS following transit of the electrolyte drop, Dielectric functions of the P3MEEMT films, In-situ ellipsometry analysis of film swelling, GIWAXS as a function of relative humidity, output and transfer curves of typical OECTs, linear mobility analysis, comparison of charge density with dielectric function, linear mobility vs charge density, normal incidence reflectance vs applied potential, summary results for films annealed at 115 °C in 0.1 mol/L KPF<sub>6</sub> and 115 ° in 0.1 mol/L KCl. Tabulated diffraction feature positions and widths as a function of relative humidity and doping potential.

## AUTHOR INFORMATION

	orcidid
Lucas Q. Flagg	0000-0002-2798-5650
Lauren E. Asselta	
Nicholas D'Antona	0000-0002-7859-7041
Tommaso Nicolini	0000-0002-9218-4702
Natalie Stingelin-Stutzmann	0000-0002-1414-4545
Jonathan W. Onorato	0000-0003-1349-8277
Christine K. Luscombe	0000-0001-7456-1343
Ruipeng Li	
Lee J. Richter	0000-0002-9433-3724

## Notes

Certain commercial equipment, instruments, or materials are identified in this paper in order to specify the experimental procedure adequately. Such identification is not intended to imply recommendation or endorsement by the National Institute of Standards and Technology (NIST), nor is it intended to imply that the materials or equipment identified are necessarily the best available for the purpose.

The authors declare no competing financial interests.

## ACKNOWLEDGMENTS

LQF acknowledges the support of a NIST-National Research Council fellowship. LA a NIST-Montgomery College internship, ND'A a NIST summer undergraduate research fellowship. JO

acknowledges the National Science Foundation (NSF) CBET-1922259 for support. This research used beamline 11BM (CMS) of the National Synchrotron Light Source a US Department of Energy (DOE) Office of Science User Facility operated for the DOE Office of Science by Brookhaven National Laboratory under contract No. DE-SC0012704. We thank Sara Orski for size-exclusion chromatography studies of the P3MEEMT. TN and NS are grateful for the financial support provided by the IONBIKE RISE project, which has received funding from the European Union's Horizon 2020 research and innovation program under the Horizon 2020 RISE Marie Skłodowska-Curie grant agreement No. 823989. TN and NS also acknowledge funding from the MARBLE project (IdEX).

## REFERENCES

(1) Rivnay, J.; Inal, S.; Salleo, A.; Owens, R. M.; Berggren, M.; Malliaras, G. G. Organic Electrochemical Transistors. *Nat. Rev. Mater.* **2018**, 3. <https://doi.org/10.1038/natrevmats.2017.86>.

(2) Paulsen, B. D.; Fabiano, S.; Rivnay, J. Mixed Ionic-Electronic Transport in Polymers. **2021**, 1–27.

(3) Moser, M.; Ponder, J. F.; Wadsworth, A.; Giovannitti, A.; McCulloch, I. Materials in Organic Electrochemical Transistors for Bioelectronic Applications: Past, Present, and Future. *Adv. Funct. Mater.* **2019**, 29 (21), 1–15. <https://doi.org/10.1002/adfm.201807033>.

(4) Guo, K.; Wustoni, S.; Koklu, A.; Díaz-Galicia, E.; Moser, M.; Hama, A.; Alqahtani, A. A.; Ahmad, A. N.; Alhamlan, F. S.; Shuaib, M.; Pain, A.; McCulloch, I.; Arold, S. T.; Grünberg, R.; Inal, S. Rapid Single-Molecule Detection of COVID-19 and MERS Antigens via Nanobody-Functionalized Organic Electrochemical Transistors. *Nat. Biomed. Eng.* **2021**, 5 (7), 666–677. <https://doi.org/10.1038/s41551-021-00734-9>.

(5) Nawaz, A.; Liu, Q.; Leong, W. L.; Fairfull-Smith, K. E.; Sonar, P. Organic Electrochemical Transistors for In Vivo Bioelectronics. *Adv. Mater.* **2021**, 2101874. <https://doi.org/10.1002/adma.202101874>.

(6) Moia, D.; Giovannitti, A.; Szumska, A. A.; Schnurr, M.; Rezasoltani, E.; Maria, I. P.; Barnes, P. R. F.; McCulloch, I.; Nelson, J. A Salt Water Battery with High Stability and Charging Rates Made from Solution Processed Conjugated Polymers with Polar Side Chains. **2017**, 1–62.

(7) Tan, S. T. M.; Quill, T. J.; Moser, M.; LeCroy, G.; Chen, X.; Wu, Y.; Takacs, C. J.; Salleo, A.; Giovannitti, A. Redox-Active Polymers Designed for the Circular Economy of Energy

Storage Devices. *ACS Energy Lett.* **2021**, *6* (10), 3450–3457.  
<https://doi.org/10.1021/acsenergylett.1c01625>.

(8) van de Burgt, Y.; Melianas, A.; Keene, S. T.; Malliaras, G.; Salleo, A. Organic Electronics for Neuromorphic Computing. *Nat. Electron.* **2018**, *1* (7), 386–397.  
<https://doi.org/10.1038/s41928-018-0103-3>.

(9) Ji, X.; Paulsen, B. D.; Chik, G. K. K.; Wu, R.; Yin, Y.; Chan, P. K. L.; Rivnay, J. Mimicking Associative Learning Using an Ion-Trapping Non-Volatile Synaptic Organic Electrochemical Transistor. *Nat. Commun.* **2021**, *12* (1), 2480.  
<https://doi.org/10.1038/s41467-021-22680-5>.

(10) Flagg, L. Q.; Bischak, C. G.; Onorato, J. W.; Rashid, R. B.; Luscombe, C. K.; Ginger, D. S. Polymer Crystallinity Controls Water Uptake in Glycol Side-Chain Polymer Organic Electrochemical Transistors. *J. Am. Chem. Soc.* **2019**, *141* (10), 4345–4354.  
<https://doi.org/10.1021/jacs.8b12640>.

(11) Giovannitti, A.; Rashid, R. B.; Thiburce, Q.; Paulsen, B. D.; Cendra, C.; Thorley, K.; Moia, D.; Mefford, J. T.; Hanifi, D.; Weiyuan, D.; Moser, M.; Salleo, A.; Nelson, J.; McCulloch, I.; Rivnay, J. Energetic Control of Redox-Active Polymers toward Safe Organic Bioelectronic Materials. *Adv. Mater.* **2020**, *32* (16), 1–9.  
<https://doi.org/10.1002/adma.201908047>.

(12) Giovannitti, A.; Nielsen, C. B.; Sbircea, D. T.; Inal, S.; Donahue, M.; Niazi, M. R.; Hanifi, D. A.; Amassian, A.; Malliaras, G. G.; Rivnay, J.; McCulloch, I. Erratum: N-Type Organic Electrochemical Transistors with Stability in Water (Nature Communications (2016) 7 (13066) DOI: 10.1038/ncomms13066). *Nat. Commun.* **2016**, *7*, 1–9.  
<https://doi.org/10.1038/ncomms13066>.

(13) Noriega, R.; Salleo, A.; Spakowitz, A. J. Chain Conformations Dictate Multiscale Charge Transport Phenomena in Disordered Semiconducting Polymers. *Proc. Natl. Acad. Sci. U. S. A.* **2013**, *110* (41), 16315–16320. <https://doi.org/10.1073/pnas.1307158110>.

(14) Venkateshvaran, D.; Nikolka, M.; Sadhanala, A.; Lemaur, V.; Zelazny, M.; Kepa, M.; Hurhangee, M.; Kronemeijer, A. J.; Pecunia, V.; Nasrallah, I.; Romanov, I.; Broch, K.; McCulloch, I.; Emin, D.; Olivier, Y.; Cornil, J.; Beljonne, D.; Sirringhaus, H. Approaching Disorder-Free Transport in High-Mobility Conjugated Polymers. *Nature* **2014**, *515* (7527), 384–388. <https://doi.org/10.1038/nature13854>.

(15) Himmelberger, S.; Vandewal, K.; Fei, Z.; Heeney, M.; Salleo, A. Role of Molecular Weight Distribution on Charge Transport in Semiconducting Polymers. *Macromolecules* **2014**, *47* (20), 7151–7157. <https://doi.org/10.1021/ma501508j>.

(16) Gu, K.; Snyder, C. R.; Onorato, J.; Luscombe, C. K.; Bosse, A. W.; Loo, Y. L. Assessing the Huang-Brown Description of Tie Chains for Charge Transport in Conjugated Polymers. *ACS Macro Lett.* **2018**, *7* (11), 1333–1338. <https://doi.org/10.1021/acsmacrolett.8b00626>.

(17) Peterson, K. A.; Thomas, E. M.; Chabinyc, M. L. Thermoelectric Properties of Semiconducting Polymers. *Annu. Rev. Mater. Res.* **2020**, *50*, 551–574. <https://doi.org/10.1146/annurev-matsci-082219-024716>.

(18) Kim, S. H.; Hong, K.; Xie, W.; Lee, K. H.; Zhang, S.; Lodge, T. P.; Frisbie, C. D. Electrolyte-Gated Transistors for Organic and Printed Electronics. *Adv. Mater.* **2013**, *25* (13), 1822–1846. <https://doi.org/10.1002/adma.201202790>.

(19) Thomas, E. M.; Brady, M. A.; Nakayama, H.; Popere, B. C.; Segalman, R. A.; Chabinyc, M. L. X-Ray Scattering Reveals Ion-Induced Microstructural Changes During Electrochemical Gating of Poly(3-Hexylthiophene). *Adv. Funct. Mater.* **2018**, *28* (44), 1–8.

https://doi.org/10.1002/adfm.201803687.

(20) Savva, A.; Cendra, C.; Giugni, A.; Torre, B.; Surgailis, J.; Ohayon, D.; Giovannitti, A.; McCulloch, I.; Di Fabrizio, E.; Salleo, A.; Rivnay, J.; Inal, S. Influence of Water on the Performance of Organic Electrochemical Transistors. *Chem. Mater.* **2019**, *31* (3), 927–937. <https://doi.org/10.1021/acs.chemmater.8b04335>.

(21) Cendra, C.; Giovannitti, A.; Savva, A.; Venkatraman, V.; McCulloch, I.; Salleo, A.; Inal, S.; Rivnay, J. Role of the Anion on the Transport and Structure of Organic Mixed Conductors. *Adv. Funct. Mater.* **2019**, *29* (5), 1–11. <https://doi.org/10.1002/adfm.201807034>.

(22) Flagg, L. Q.; Bischak, C. G.; Quezada, R. J.; Onorato, J. W.; Luscombe, C. K.; Ginger, D. S. P-Type Electrochemical Doping Can Occur by Cation Expulsion in a High-Performing Polymer for Organic Electrochemical Transistors. *ACS Mater. Lett.* **2020**, *2* (3), 254–260. <https://doi.org/10.1021/acsmaterialslett.9b00501>.

(23) Moser, M.; Hidalgo, T. C.; Surgailis, J.; Gladisch, J.; Ghosh, S.; Sheelamanthula, R.; Thiburce, Q.; Giovannitti, A.; Salleo, A.; Gasparini, N.; Wadsworth, A.; Zozoulenko, I.; Berggren, M.; Stavrinidou, E.; Inal, S.; McCulloch, I. Side Chain Redistribution as a Strategy to Boost Organic Electrochemical Transistor Performance and Stability. *Adv. Mater.* **2020**, *32* (37), 1–6. <https://doi.org/10.1002/adma.202002748>.

(24) Bihar, E.; Deng, Y.; Miyake, T.; Saadaoui, M.; Malliaras, G. G.; Rolandi, M. A Disposable Paper Breathalyzer with an Alcohol Sensing Organic Electrochemical Transistor. *Sci. Rep.* **2016**, *6* (December 2015), 2–7. <https://doi.org/10.1038/srep27582>.

(25) Nicolini, T.; Surgailis, J.; Savva, A.; Scaccabarozzi, A. D.; Nakar, R.; Thuau, D.; Wantz, G.; Richter, L. J.; Dautel, O.; Hadzioannou, G.; Stingelin, N. A Low-Swelling Polymeric

Mixed Conductor Operating in Aqueous Electrolytes. *Adv. Mater.* **2021**, *33* (2), 2005723. <https://doi.org/10.1002/adma.202005723>.

(26) Paulsen, B. D.; Wu, R.; Takacs, C. J.; Steinrück, H.; Strzalka, J.; Zhang, Q.; Toney, M. F.; Rivnay, J. Time-Resolved Structural Kinetics of an Organic Mixed Ionic–Electronic Conductor. *Adv. Mater.* **2020**, *32* (40), 2003404. <https://doi.org/10.1002/adma.202003404>.

(27) Wu, R.; Matta, M.; Paulsen, B. D.; Rivnay, J. Operando Characterization of Organic Mixed Ionic/Electronic Conducting Materials. *Chem. Rev.* **2022**, *122* (4), 4493–4551. <https://doi.org/10.1021/acs.chemrev.1c00597>.

(28) Wu, C. H.; Weatherup, R. S.; Salmeron, M. B. Probing Electrode/Electrolyte Interfaces in Situ by X-Ray Spectroscopies: Old Methods, New Tricks. *Phys. Chem. Chem. Phys.* **2015**, *17* (45), 30229–30239. <https://doi.org/10.1039/c5cp04058b>.

(29) Koop, T.; Schindler, W.; Kazimirov, A.; Scherb, G.; Zegenhagen, J.; Schulz, T.; Feidenhans', R.; Kirschner, J. Electrochemical Cell for in Situ X-Ray Diffraction under Ultrapure Conditions. *Rev. Sci. Instrum.* **1998**, *69* (4), 1840–1843. <https://doi.org/10.1063/1.1148852>.

(30) Wang, J.; Ocko, B. M.; Davenport, A. J.; Isaacs, H. S. In Situ X-Ray-Diffraction and - Reflectivity Studies of the Au(111)/Electrolyte Interface: Reconstruction and Anion Adsorption. *Phys. Rev. B* **1992**, *46* (16), 10321–10338. <https://doi.org/10.1103/PhysRevB.46.10321>.

(31) Herron, M. E.; Doyle, S. E.; Roberts, K. J.; Robinson, J.; Walsh, F. C. Instrumentation and Cell Design for in Situ Studies of Electrode Surfaces Using X-Ray Synchrotron Radiation. *Rev. Sci. Instrum.* **1992**, *63* (1), 950–955. <https://doi.org/10.1063/1.1143789>.

(32) Samant, M. G.; Toney, M. F.; Borges, G. L.; Blum, L.; Melroy, O. R. In-Situ Grazing

Incidence X-Ray Diffraction Study of Electrochemically Deposited Pb Monolayers on Ag(111). *Surf. Sci.* **1988**, *193* (1–2), L29–L36. [https://doi.org/10.1016/0039-6028\(88\)90314-7](https://doi.org/10.1016/0039-6028(88)90314-7).

(33) Bischak, C. G.; Flagg, L. Q.; Yan, K.; Rehman, T.; Davies, D. W.; Quezada, R. J.; Onorato, J. W.; Luscombe, C. K.; Diao, Y.; Li, C.-Z. Z.; Ginger, D. S. A Reversible Structural Phase Transition by Electrochemically-Driven Ion Injection into a Conjugated Polymer. *J. Am. Chem. Soc.* **2020**, *142* (16), 7434–7442. <https://doi.org/10.1021/jacs.9b12769>.

(34) Paulsen, B. D.; Giovannitti, A.; Wu, R.; Strzalka, J.; Zhang, Q.; Rivnay, J.; Takacs, C. J. Electrochemistry of Thin Films with In Situ/Operando Grazing Incidence X-Ray Scattering: Bypassing Electrolyte Scattering for High Fidelity Time Resolved Studies. *Small* **2021**, *17* (42), 2103213. <https://doi.org/10.1002/smll.202103213>.

(35) Richter, L. J.; Delongchamp, D. M.; Amassian, A. Morphology Development in Solution-Processed Functional Organic Blend Films: An in Situ Viewpoint. *Chem. Rev.* **2017**, *117* (9), 6332–6366. <https://doi.org/10.1021/acs.chemrev.6b00618>.

(36) Inal, S.; Malliaras, G. G.; Rivnay, J. Benchmarking Organic Mixed Conductors for Transistors. *Nat. Commun.* **2017**, *8* (1), 1–6. <https://doi.org/10.1038/s41467-017-01812-w>.

(37) Flagg, L. Q.; Giridharagopal, R.; Guo, J.; Ginger, D. S. Anion-Dependent Doping and Charge Transport in Organic Electrochemical Transistors. *Chem. Mater.* **2018**, *30* (15), 5380–5389. <https://doi.org/10.1021/acs.chemmater.8b02220>.

(38) Snowden, M. E.; Güell, A. G.; Lai, S. C. S.; McKelvey, K.; Ebejer, N.; O’Connell, M. A.; Colburn, A. W.; Unwin, P. R. Scanning Electrochemical Cell Microscopy: Theory and Experiment for Quantitative High Resolution Spatially-Resolved Voltammetry and Simultaneous Ion-Conductance Measurements. *Anal. Chem.* **2012**, *84* (5), 2483–2491.

https://doi.org/10.1021/ac203195h.

(39) Stafford, C. M.; Roskov, K. E.; Epps, T. H.; Fasolka, M. J. Generating Thickness Gradients of Thin Polymer Films via Flow Coating. *Rev. Sci. Instrum.* **2006**, *77* (2), 1–7. <https://doi.org/10.1063/1.2173072>.

(40) Kayunkid, N.; Uttiya, S.; Brinkmann, M. Structural Model of Regioregular Poly(3-Hexylthiophene) Obtained by Electron Diffraction Analysis. *Macromolecules* **2010**, *43* (11), 4961–4967. <https://doi.org/10.1021/ma100551m>.

(41) Lim, E.; Glaudell, A. M.; Miller, R.; Chabiny, M. L. The Role of Ordering on the Thermoelectric Properties of Blends of Regioregular and Regiorandom Poly(3-hexylthiophene). *Adv. Electron. Mater.* **2019**, *5* (11), 1800915. <https://doi.org/10.1002/aelm.201800915>.

(42) Schroeder, P. von. Über Erstarrungs- Und Quellungserscheinungen von Gelatine. *Zeitschrift für Phys. Chemie* **1903**, *45U* (1), 75–117. <https://doi.org/10.1515/zpch-1903-4503>.

(43) Weber, A. Z.; Newman, J. Transport in Polymer-Electrolyte Membranes. *J. Electrochem. Soc.* **2004**, *151* (2), A311. <https://doi.org/10.1149/1.1639157>.

(44) Thelen, J. L.; Wu, S.-L.; Javier, A. E.; Srinivasan, V.; Balsara, N. P.; Patel, S. N. Relationship between Mobility and Lattice Strain in Electrochemically Doped Poly(3-Hexylthiophene). *ACS Macro Lett.* **2015**, *4* (12), 1386–1391. <https://doi.org/10.1021/acsmacrolett.5b00827>.

(45) Guardado, J. O.; Salleo, A. Structural Effects of Gating Poly(3-hexylthiophene) through an Ionic Liquid. *Adv. Funct. Mater.* **2017**, *27* (32), 1701791. <https://doi.org/10.1002/adfm.201701791>.

(46) Wang, S.; Ha, M.; Manno, M.; Daniel Frisbie, C.; Leighton, C. Hopping Transport and the

Hall Effect near the Insulator–Metal Transition in Electrochemically Gated Poly(3-Hexylthiophene) Transistors. *Nat. Commun.* **2012**, *3* (1), 1210. <https://doi.org/10.1038/ncomms2213>.

(47) Bittle, E. G.; Ro, H. W.; Snyder, C. R.; Engmann, S.; Kline, R. J.; Zhang, X.; Jurchescu, O. D.; DeLongchamp, D. M.; Gundlach, D. J. Dependence of Electrical Performance on Structural Organization in Polymer Field Effect Transistors. *J. Polym. Sci. Part B Polym. Phys.* **2017**, *55* (14), 1063–1074. <https://doi.org/10.1002/polb.24358>.

(48) Lim, E.; Peterson, K. A.; Su, G. M.; Chabinyc, M. L. Thermoelectric Properties of Poly(3-Hexylthiophene) (P3HT) Doped with 2,3,5,6-Tetrafluoro-7,7,8,8-Tetracyanoquinodimethane (F4TCNQ) by Vapor-Phase Infiltration. *Chem. Mater.* **2018**, *30* (3), 998–1010. <https://doi.org/10.1021/acs.chemmater.7b04849>.

## TOC GRAPHICS

